

MACH-ZEHNDER WAVEFRONT SENSOR FOR PHASING OF SEGMENTED TELESCOPES

L. Montoya Martinez^{*a}, N. Yaitskova^{**b}, P. Dierickx^{**b}, K. Dohlen^{*a}

^aLaboratoire d'Astrophysique de Marseille

^bEuropean Southern Observatory

ABSTRACT

Segmented mirror technology has been successfully applied to 10m class telescopes (Keck, HET, GTC) and is widely recognized as mandatory for Extremely Large Telescopes. For optimal performance the wavefront error associated with segmentation should remain within conservative limits, typically $1/20^{\text{th}}$ of a wave. Several phasing techniques and associated metrologies are under development, with a view to extrapolate such methods to the 100-m OWL telescope. We investigate a novel technique based on Mach-Zehnder interferometry, whereby the wavefront in one of the interferometer arms is spatially filtered so as to provide a reference wave, prior to having the two arms recombined to produce suitable interferograms. We introduce a theoretical description of the interferometer, as well as results of simulations, showing that with proper settings of the interferometer's parameters, the technique can be made insensitive to atmospheric turbulence and, more generally, to almost any error source not associated with the segmentation. It also appears that, in a telescope that would include more than one segmented mirror, simple processing allows to disentangle the signal associated to each of them. Finally, we outline the development still required to complete a full qualification of this approach.

Keywords: phasing, segmented mirrors, OWL, Mach-Zehnder interferometry.

1. INTRODUCTION

Optical segmentation is widely recognized as prerequisite to extrapolating telescope sizes much beyond current figures. While the technology has been successfully demonstrated with the Keck 10-m telescopes, Extremely Large Telescopes (ELTs) will require a one to two orders of magnitude increase in the number of segments, hence in the number of degrees of freedom to be controlled reliably and accurately. The techniques generally promoted for ELTs are, in their principle, identical to that routinely implemented in the Keck. Position sensors conveniently located at the back or the edges of the segments provide, in real time, measurements of the inter-segments steps, down to a few nanometers accuracy. Whichever technology such sensors rely on, periodic calibration of their readings appears necessary. This calibration is ideally performed on-sky; Chanan et al¹ have successfully developed a wavefront sensing technique which allows re-calibration of the Keck sensors, within adequate accuracy and at an affordable cost in terms of operational overheads –typically a few hours on a monthly basis. The technique seems scalable to a very large number of segments, within existing technology¹. In the case of OWL, which has segmented primary and secondary mirrors, the technique would most likely require two wavefront sensors, each fitted with proper pupil masks centered on the images of segment boundaries. Those would provide independent calibrations of each segmented mirror.

Even though the progress of sensor technologies should logically lead to better temporal stability than in the Keck, ELTs are required to routinely achieve diffraction-limited resolution, thus implying tighter phasing requirements and lower allowances for sensor drift. In addition, the Keck technique implies a tight centering of the pupil mask in the wavefront sensor and requires relatively bright stars. Even though improvements seem possible, as proposed by the Gran Telescopio de Canarias (GTC) team², there are strong incentives to develop alternative calibration techniques.

Within the framework of a European Community-funded Research and Training Network (RTN) on adaptive optics for Extremely Large Telescopes, the Laboratoire d'Astrophysique de Marseille and the European Southern Observatory are jointly evaluating a technique based on Mach-Zehnder interferometry. This is one of several alternatives explored by the Network, which is in the process of establishing a comprehensive review of possible phasing techniques. Different techniques are evaluated with respect to accuracy, capture range, reference source brightness, sensitivity to wavefront errors not directly related to segmentation, sensor complexity and tolerances, and operational overheads. In the following, and after detailing its theoretical properties, we will use simulations to show that a properly tuned Mach-Zehnder interferometer is relatively insensitive to atmospheric turbulence and any error source of lower spatial

frequency, thus allowing it to measure phasing errors on seeing-limited star images and, by implication, on strongly aberrated images. We will also provide results indicating that the signal could easily be processed to deliver the phasing information associated to multiple segmentation, as required in the 100-m OWL telescope. Although a complete characterization of the sensor still requires proper evaluation of tolerances and of practical implementation aspects, current results suggest that a sensor tailored to OWL properties could be built using readily available technology.

2. MACH-ZEHNDER COPHASING SENSOR CONCEPT

2.1 Concept overview

The purpose of the Mach-Zehnder wavefront sensor is to measure phase properties of the incoming wavefront by applying appropriate spatial filtering in one of the interferometer arms. In practice, this can be done by making sure the beam goes through a focus within the interferometer, as shown in Fig.1. The idea to use this kind of interferometer to measure atmospheric wavefront errors was first introduced by Angel³. A pinhole of size (as projected onto the sky) of the order of λ/D , where D is the telescope diameter, is placed in the focal plane of one of the arms, producing a spherical wavefront. When recombined with the wavefront coming from the other arm an interferogram is produced, from which atmospheric errors can be deduced. However, when atmospheric aberrations are large, this technique becomes very inefficient since the pinhole is much smaller than the seeing disk. Also, the number of fringes is large, making interferogram analysis very difficult.

We propose to use a modified version of this technique for measurement of segment phasing errors. Phase steps create wavefront errors of all spatial frequencies, and, as we will show, the step-induced errors become dominant over atmospheric errors for spatial frequencies higher than about λ/r_0 . Increasing the pinhole size to about the size of the seeing disk allows to cancel out phase errors due to the atmosphere while retaining enough information about phase steps to generate a useful signal. Fig. 2 illustrates the selective blurring effect of increasing the pinhole size. In this simulation, we generated an arbitrary wavefront, and calculated the interferograms with increasing pinhole sizes.

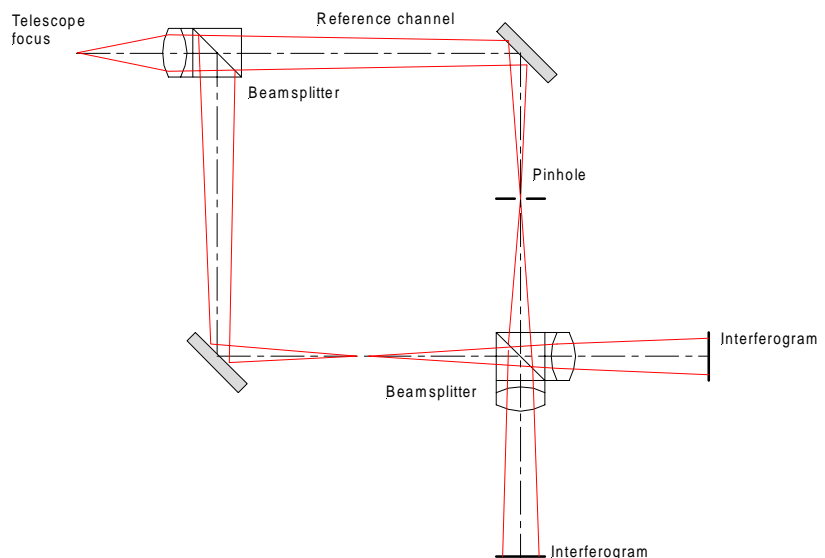


Fig1.:Layout of a Mach-Zehnder interferometer.

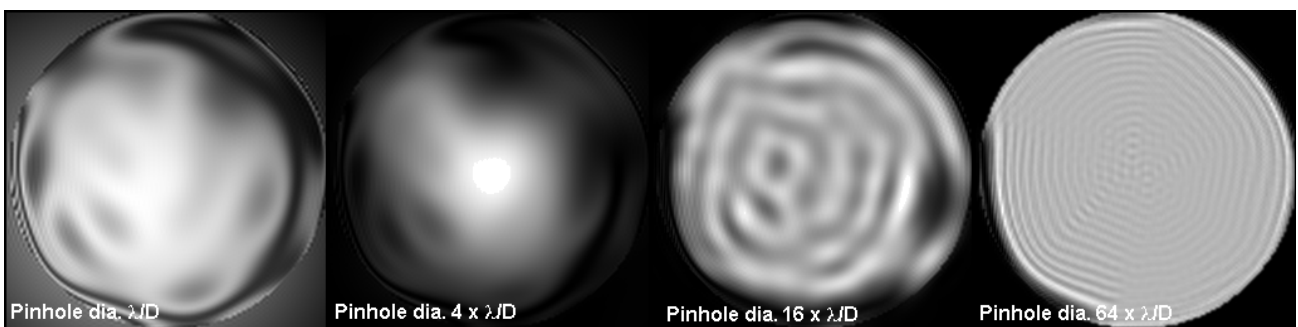


Fig.2: Simulated Mach-Zehnder interferograms in the presence of atmospheric seeing for different size of pinhole.

2.2 Theoretical analysis

One advantage of the Mach-Zehnder sensor is that the wavefront errors are measured directly from the interference pattern registered on the detectors. The intensity in the two interferograms is proportional to the cosine of the phase difference between the two arms. By conservation of energy, these two patterns are complementary when the beam-splitter is non-absorbing: maxima in one correspond to minima in the other. If both interferograms can be detected, calculating their difference doubles the sensitivity as compared with a single interferogram and eliminates the common background.

The two complex amplitudes at the output pupil plane are:

$$\mathbf{A}_1 = \frac{-1}{\sqrt{2}}(A'e^{i\varphi} + A''e^{i\varphi'}) \quad \mathbf{A}_2 = \frac{-1}{\sqrt{2}}(A'e^{i\varphi} - A''e^{i\varphi'})$$

where A' and φ' are the amplitude and phase of the wavefront after the pinhole and A'' and φ are the amplitude and phase of the reference wavefront.

The intensities of the interferograms are calculated as $I = |\mathbf{A}\mathbf{A}^*|^2$

$$I_2 = \left(\frac{I'}{2} + \frac{I''}{2}\right)(1 - V \cos(\varphi - \varphi')) \quad I_1 = \left(\frac{I'}{2} + \frac{I''}{2}\right)(1 + V \cos(\varphi - \varphi'))$$

where $I' = A'^2$ is the intensity after the pinhole in one of the arms, $I'' = A''^2$ is the intensity in the other arm before recombination, and V is the visibility of the fringes in the output pupil plane. As expected, the intensities of the interferograms are, apart from a constant, proportional to the cosine of the phase difference.

From these interferograms we can not retrieve the sign of the phase because of the symmetry of the *cosine* function, $\cos(\varphi - \varphi') = \cos(\varphi' - \varphi)$. This problem can be solved if a constant optical path difference (OPD) is introduced in one of the arms. If the OPD = $\lambda/4$, corresponding to a phase difference of $\pi/2$, the intensities are proportional to $\cos(\varphi - \varphi' + \pi/2) = \sin(\varphi - \varphi')$, and the anti symmetry of the *sine* function permits the sign distinction, $\sin(\varphi - \varphi') = -\sin(\varphi' - \varphi)$.

As discussed in section 2.1 the pinhole acts as a low pass spatial filter in one of the arms. When the two wavefront coming from two arms recombine the whole Mach-Zehnder acts as a high pass filter. In this sense this type of Mach-Zehnder sensor is equivalent to a Smartt interferometer or a stellar coronagraph.

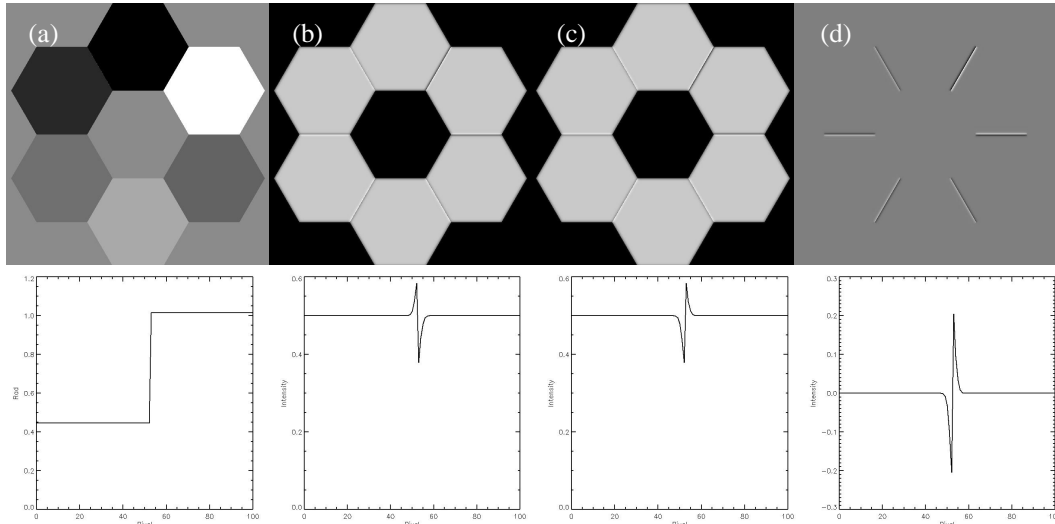


Fig3: Mach Zehnder simulation for segmented mirror with random rms piston error of $\lambda/8$ and pin hole size=2.3", (a)input wavefront,(b) Interferogram output 1,(c)Interferogram output 2,(d) difference between interferograms. The lower row represents a transversal cut along the segment edge.

3. PERFORMANCE OF A MACH-ZEHNDER PHASING INTERFEROMETER

In this section we explore the effect of some of the parameters of the Mach-Zehnder wavefront sensor. Those parameters are the shape and size of the pinhole, which are directly related to the pupil sampling, and the optical path difference (OPD) between two arms of the interferometer. The goal is to find an optimal configuration to extract the phase errors with the maximal accuracy.

For this purpose we have simulated a segmented pupil with seven 0.9m side hexagonal mirrors with random piston errors. In Fig.3 we show an example of this configuration, in the left we show the input wavefront for a segmented pupil with random piston error of $\lambda/8$ with $\lambda=0.656 \mu\text{m}$. In the middle we plot the two outputs interferograms, using a pinhole size 100 times the size of the airy disk ($100\lambda/D \approx 2.3''$). On the right the difference between the two interferograms is plotted. We are interested in the profile of the interferogram along the segment edge, as plotted at the bottom of Fig.3.

3.1 Pinhole profile

To avoid diffraction artefacts associated to the pinhole sharp edge, the circular top hat mask may be replaced with an apodized mask with a Gaussian profile. The comparison of illumination profiles for the two mask types is shown in Fig.4. Segment piston in both cases is $\lambda/6$, wavefront. The FWHM of the Gaussian mask is equal to the diameter of the top hat mask in the first case. Diffraction artefacts are clearly eliminated with a pinhole having a gaussian profile.

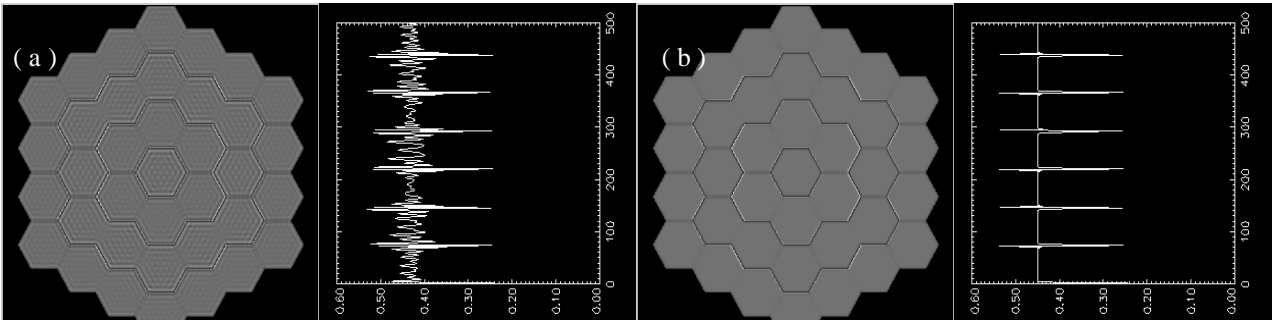


Fig.4: Comparison between the Mach Zehnder interferogram using a pinhole with circular shape (a) and pinhole with gaussian shape (b). A transversal cut along the main y-axis of the interferogram shows the elimination of bound effect.

3.2 Mask size, pupil sampling

The optimal pinhole size is defined by the number of pixels required to resolve the signal profile and by the range of frequencies to be spatially filtered. Pupil sampling and pinhole size are evidently correlated, as the pinhole acts as aperture for the pupil imaging system. The smaller the pinhole size, the larger the Point Spread Function (PSF) of this system is, hence the larger the width of the signal profile. This relation is illustrated by plotting the width of the signal fluctuation as a function of the inverse of the pinhole size, Fig.5.

We find a linear relation between the size of the pinhole and the width of the profile, shown in Fig.6. To resolve the profile signal at least 4 pixels are required. This means the diameter of the hole should be less than $0.8304 \lambda/D$, where N is the number of pixels across the interferogram, λ is the wavelength and D is the pupil diameter. For OWL, with a primary of $D = 100\text{m}$, and assuming $\lambda = 500\text{nm}$, the pinhole should be smaller than $1.65''$ for a $2\text{K} \times 2\text{K}$ detector. For a $4\text{K} \times 4\text{K}$ detector the maximal size is $3.3''$. If we want to blur the effect of atmospheric turbulence, the hole size will also depend on the size of λ/r_0 (we will come back later to this point).

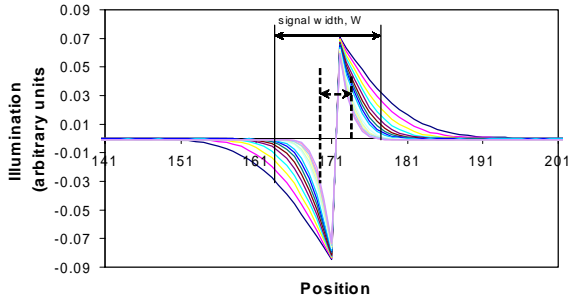


Fig.5: Intersegment illumination for different size of pinhole from FWHM=2'' to FWHM=0.5''.

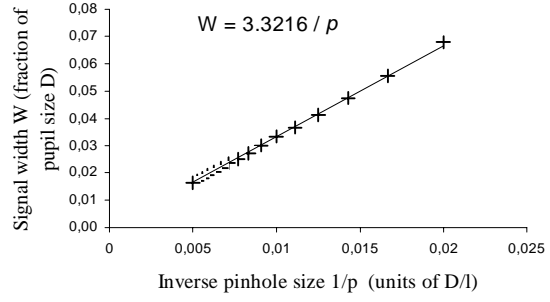


Fig.6: Linearity of width of interference profile with pinhole size.

3.3 Phase retrieval algorithm

In this section we introduce an OPD between the two arms of the interferometer and we describe a simple algorithm to retrieve the phase from the profile of the difference between the two outputs at the segment boundary.

In Fig.7 we show three sets of interferograms for different OPDs, conveniently introduced as a constant phase shift in the reference arm of the interferometer. From left to right, the figure shows the interferogram profiles for the two outputs and their difference (referred to as differential interferogram). At zero OPD (upper row) the phase information is contained within a distinct peak appearing at the segment boundary. The height of the peak is proportional to the square of the phase step; the sign of the phase value is therefore lost. At non-zero OPD, a signal oscillation appears at the segment edge. We refer to the amplitude of this oscillation as the peak-to-valley (PtV) value. In Fig.8 we show the PtV value as a function of OPD for $\lambda=0.656\mu\text{m}$. The phase shift $\lambda/4$ (or $3\lambda/4$, due to the symmetry) allows achieving

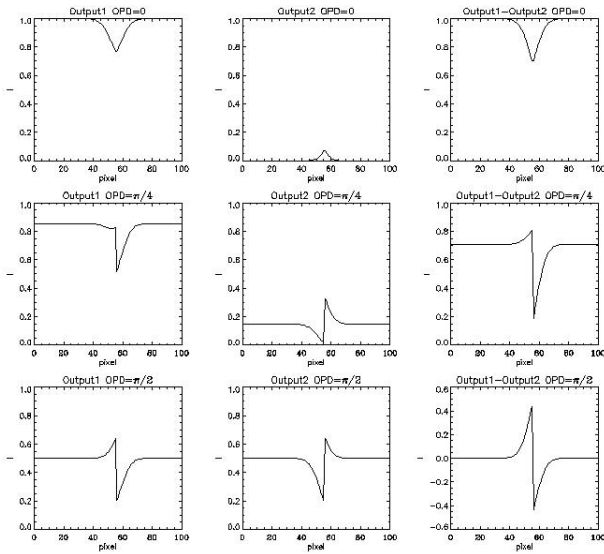


Fig.7: Profile of the two outputs interferograms (column 1 and 2) and difference of interferograms (column 3) at the segment edge for different OPDs.

the maximum PtV i.e., maximum contrast. As seen in the lower panel of Fig. 7, with this OPD the two interferograms have the same background level so that when we subtract them the background is eliminated.

For small intersegment steps, the PtV is proportional to the phase step between segments, representing a good estimate of residual phasing errors. In Fig.9, we plot the PtV for two wave lengths, $\lambda_1=0.656\mu\text{m}$ and $\lambda_2=0.5\mu\text{m}$. As expected these functions are of the form:

$$v(p, \lambda) = A \sin\left(2\pi \frac{OPD}{\lambda}\right) \sin\left(2\pi \frac{p}{\lambda}\right),$$

where v is the PtV value of the differential interferogram, p is the local intersegment piston and A is a coefficient which deepens on external parameters, such as pinhole size, sampling, intensity of input wave, and absorption coefficients.

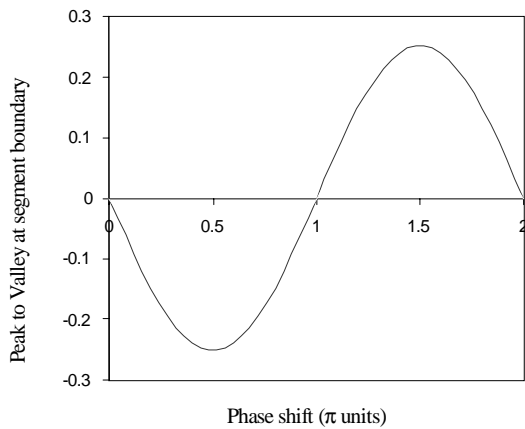


Fig.8: Peak to valley at segment boundary (signal) as a function of the phase shift (OPD), $\lambda=0.656\mu\text{m}$, piston error is $\lambda/4$ wavefront, FWHM of the pinhole is $1''$.

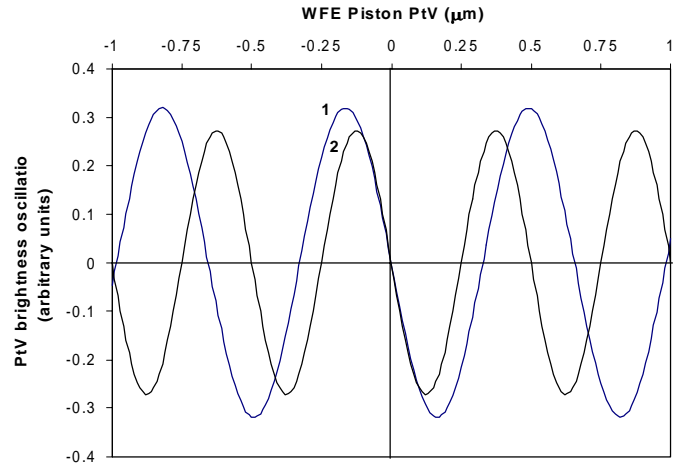


Fig.9: PtV of the oscillation across the intersegment boundary, as a function of piston for two wavelengths $\lambda_1=0.656\mu\text{m}$ (curve 1) and $\lambda_2=0.5\mu\text{m}$ (curve 2).

Due to the π ambiguity the monochromatic regime does not allow to unequivocally determine piston errors outside the range $\pm \lambda/4$. That problem can be solved by the use of two or more wavelengths. Two outputs of the interferometer give an opportunity to measure signals in two different wavelengths simultaneously. The capture range is limited by the number of wavelengths used, the measurement error² and filter bandwidth. For cophasing a capture range of the order of 5 to $10\mu\text{m}$ is desirable. If we use two wavelengths (e.g., 650nm and 840nm), the measurement error should be less than 10nm to achieve such range without ambiguities. Assuming that the Mach Zehnder sensor has a precision of about 30 nm, this means that the maximal capture range we could get with two wavelengths is $3\mu\text{m}$ and it may not be enough. If we use three wavelengths (e.g., 650nm, 795nm, 835nm), a precision of 30 nm will provide the desired range.

3.4 Pupil registration

Signal retrieval requires the precise knowledge about the location of intersegment boundary. The presence of intersegment gaps provides a convenient way to register the pupil. That can be achieved by removing the pinhole, filters and recording white light images of the pupil. These images will show the exact location of the segment boundaries and hence will indicate where the signal is to be measured. The signal being proportional to the segment gap size, its intensity is low and there are compelling reasons for enlarging the wave band as much as possible. In the case of OWL, assuming 4Kx4K detectors and $\sim 6\text{-mm}$ gap size, pixels conjugated to intersegment gaps would reveal a $\sim 25\%$ drop in an otherwise uniform signal.

In the case of OWL, there are two segmented mirrors (primary and secondary) which need to be phased independently. In the whole interferogram the two segmentation structures appear together and need to be separated. Being projected onto the pupil plane these two structures have different spatial frequencies, corresponding to different projected distance between segments. Simple Fourier filtering allows to disentangle the patterns associated to each segmented surface.

Fig.10 shows the registration image, which contains the information about the two segmented mirrors. The results of a two spatial Fourier filtering are also shown, the filters being tailored to the geometry of each segmented surface. In each case the “undesired” structure has almost disappeared.

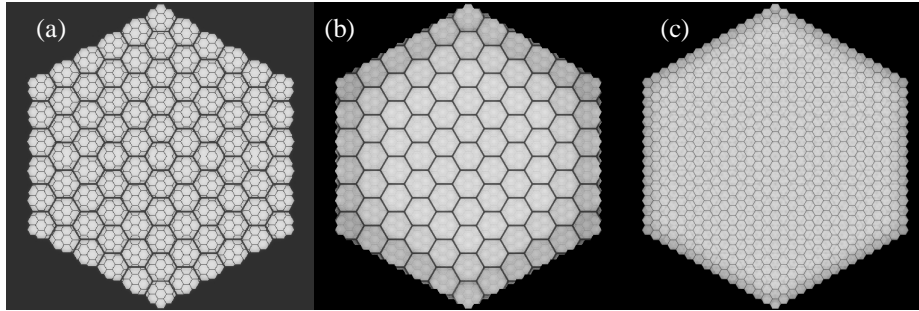


Fig.10: Interferogram of two mirrors before (a) and after Fourier filtering (b and c), segment size 1.5m, gap=20mm,. Waveband=[328nm,875nm]

4. ATMOSPHERIC TURBULENCE

One of the main difficulty in any cophasing method is the influence of the turbulent atmosphere. One possible but generally inconvenient option is to perform the calibration on an adaptively compensated image. Another one is to try to “beat” the atmosphere, either by using very short exposures or by retrieving the relevant information from subapertures smaller than the atmospheric coherence length. A mach-Zehnder wavefront sensor would be quite efficient in that respect, since the effect of atmospheric turbulence can already be blurred out on short exposure.

In Fig.11 we show simulated interferograms obtained with increasing pinhole width. The input wavefront is shown in Fig.11.a. It contains the atmospheric turbulence component (0.65” seeing, von Karman spectrum) and 109nm piston error (completely blurred out by the atmosphere).

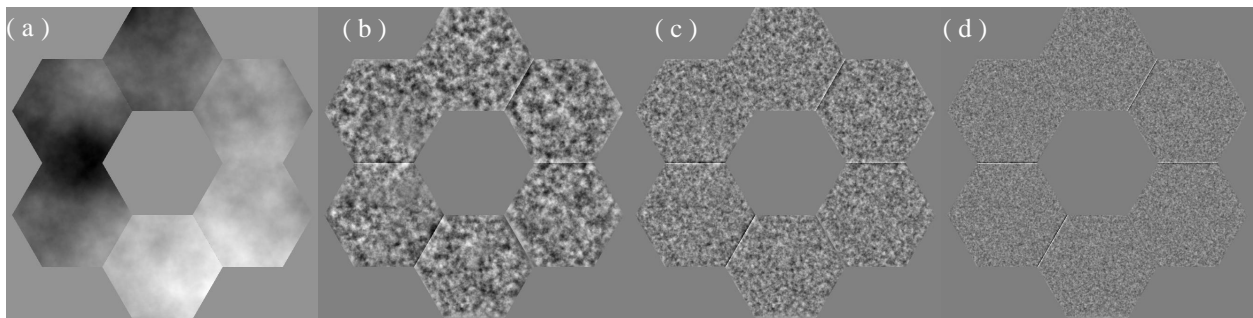


Fig.11: Wavefront containing piston error and atmospheric aberration (a). Short exposure interferogram for pinhole size 0.65” (b), 1.3” (c), 2.6” (d). Seeing 0.65”, piston error 109nm, $\lambda=0.656\mu\text{m}$.

4.1 Optimal pinhole size for short exposure image

In terms of frequencies we have to optimise the size of the hole in such way to blur out all spatial frequencies up to that of the atmospheric turbulence. In Fig.12 we show the PSF corresponding to a wavefront in presence of turbulence with a seeing equal to 0.41” (solid) and the PSF corresponding to a wavefront with a step difference between segment of $\lambda/4$ (dotted). We observe that the effect of the atmosphere (solid line) dominates up to a radius of 0.4”, while it is the effect of piston (dotted line) which dominates beyond that radius.

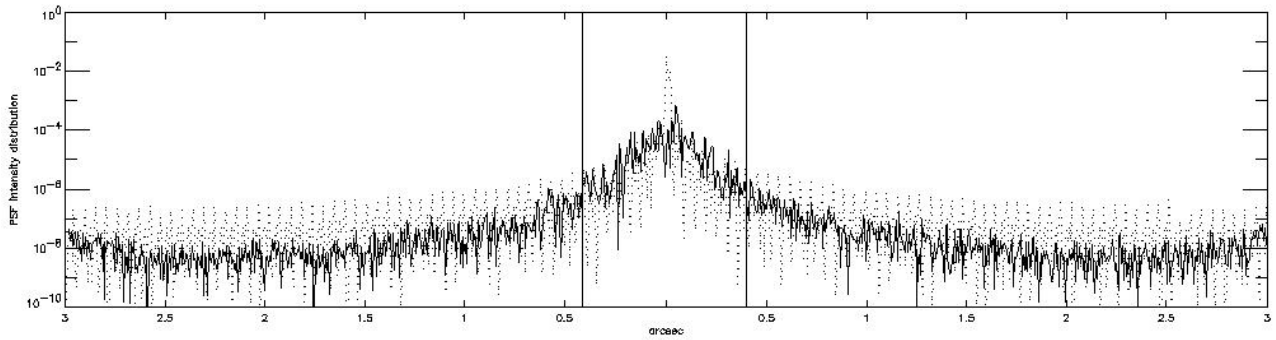


Fig.12: Intensity distribution of the PSF for an input wavefront with piston error (dotted) and atmospheric errors (solid)

In principle the size of the pinhole should be adjusted to the turbulence conditions. In Fig.13 we show the PtV value of the differential interferogram as a function of pinhole size for different atmospheric conditions. As expected the peak difference is bigger with better seeing. We also note that the optimum size of the hole increases as the turbulence becomes worse.

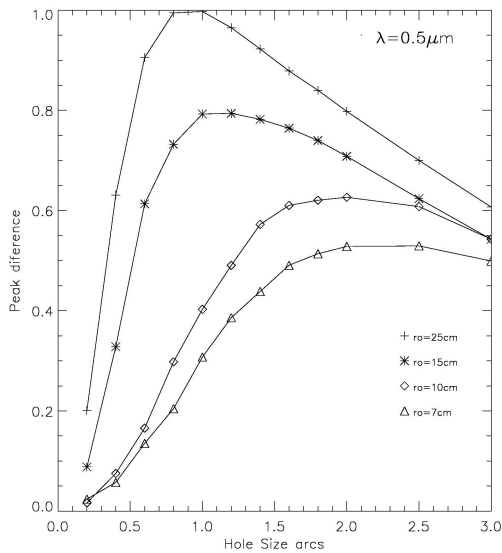


Fig.13: PtV value of the differential interferogram for different size of r_0 .

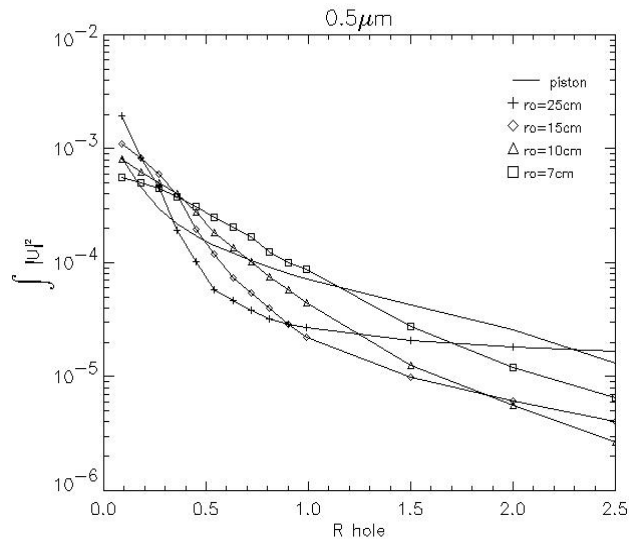


Fig.14: Total energy as a function of pinhole size.

We have calculated the total energy in the focal plane that comes through the hole for different turbulence conditions, changing the size of the hole. If the size of the pinhole is smaller than the size of the atmosphere (λ/r_0) the total energy due to the atmosphere is bigger than the total energy due to piston errors. For each atmospheric condition there is a hole size where this relation is reversed and the energy due to piston becomes higher than that associated to atmosphere. This is shown in Fig.14.

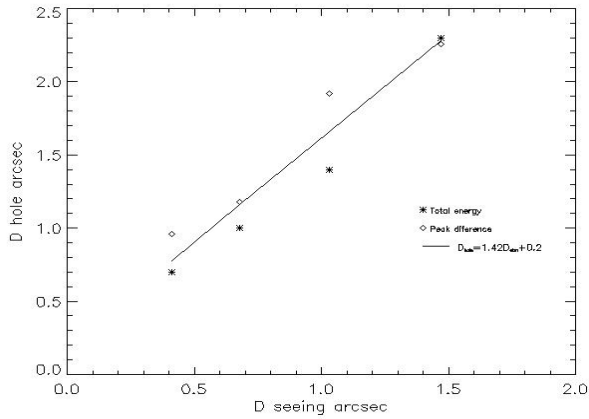


Fig.15: Linear relation between the size of the seeing disk and the optimal pinhole size.

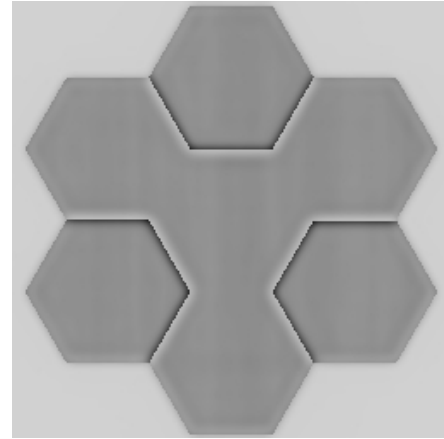


Fig.16: Long exposure signal with 0.65'' seeing and 80nm piston

In Fig.15 we plot the optimal pinhole diameter for different values of seeing. We choose two different criteria, one is the maximal value of the PtV in the differential interferogram obtained from Fig 13, and the other is the point where the total energy coming through the hole is dominated by piston (Fig.14). A linear fitting gives the following relation between the optimal pinhole size and seeing disk,

$$D_{\text{pinhole}} = 1.42 D_{\text{atm}} + 0.2$$

where $D_{\text{atm}} = \lambda/r_0$ in arcsec and D_{pinhole} is the diameter of pinhole.

4.2 Long exposure image

Long exposure imaging can provide better contrast for the signal and allows to use fainter reference sources. Fig.16 shows the illumination profile obtained after 5min exposure. The phase screen which presents the turbulence in this case was moving with the wind speed 5m/sec across the pupil. The background feature caused by an atmosphere, which we observed in the previous example, is in this case completely smoothed, leaving the constant background.

5. FUTURE WORK

Current results will have to be completed by a full characterization of a Mach-Zehnder wavefront sensor for the phasing of Extremely Large telescopes.

Most of this work will rely on simulations and will concentrate on expected accuracy limiting magnitude, implementation and alignment requirements, but also on the effect of segments edges misfigure. The latter is deemed as a serious weakness of this type of wavefront sensor –the reason being that such misfigure has a higher spatial frequency content than atmospheric turbulence, and may not be efficiently filtered out. Would this difficulty be eventually overcome, operational schemes will have to be explored as well.

A laboratory experiment is being assembled by the Laboratoire d'Astrophysique de Marseille. This experiment will eventually include a phase screen aimed at simulating the disturbing effect of the atmosphere. Would this experiment be concluded successfully, and under the provision that the effect of segments edge misfigure can be reasonably dealt with –i.e. by other means than unrealistically tight segments figuring tolerances, a prototype may eventually be integrate in the ESO Active Phasing Experiment (APE) and tested on the sky.

6. CONCLUSION

We have described the principle of a Mach-Zehnder wavefront sensor and shown by simulation that it may provide an efficient mean to measure inter-segments steps. The piston error is directly measured from interferograms at planes conjugated with the segmented aperture(s). By implication and taking into account the fact that the entire segmentation patterns is recorded by the cameras of the wavefront sensor, segments relative tilt may be measured as well by analysing the profile of the signal oscillation along the segments boundaries.

Introducing an OPD in one arm of the interferometer allows the contrast of the two output interferogram to be optimised and removes the sign ambiguity. Use of an amplitude mask instead of a pinhole allows to clean the interferograms from undesirable diffraction artefacts. A strong advantage of this type of wavefront sensor is its relative insensitivity to any error sources of spatial frequency lower than that to be detected, and in particular to atmospheric turbulence. Taking the latter into account, we find a minimum pinhole size or FWHM of the Gaussian filter $\sim 1.42 \lambda/r_0 + 0.2$. Using OWL aperture characteristics, we also find a practical upper size of ~ 1.65 to 3.3 arc seconds, depending on sampling, and compatible with the lower limit. The phase information can be retrieved from both short- and long-exposures, the latter delivering a better signal-to-noise ratio. Another advantage is its likely ease of implementation, no complex pupil mask being required as in the Keck¹.

ACKNOWLEDGMENT

The authors wish to acknowledge that this research is supported by the European Commission RTN program: "Adaptive Optics for the Extremely Large Telescopes", under contract #HPRN-CT-2000-00147.

REFERENCES

1. G.Chanan, M.troy, C.Ohara, "Phasing the primary mirror segments of the Keck telescopes: a comparison of different techniques", *Proc.SPIE*, **4003**, 188-201,2000.
2. A. Schumacher,N.Devaney, L.Montoya, "Phasing segmented mirrors: a modification of the Keck narrow-band technique and its application to extremely large telescopes", *Applied Optics*, **41**, 1297-1307, 2002.
3. J.R.P.Angel, "Ground-based imaging of extrasolar planets using adaptive optics", *Nature*, **368**, 203-207,1994.
4. P. Dierickx et al, "Eye of the beholder: designing the OWL", *Proc SPIE conf. on Future Giant Telescopes*,2002.

*montoya@oamp.fr; phone +34 0495044112; fax 0034 0491621190; www.oamp.fr; Laboratoire de' Astrophysique de Marseille, 2 Place Leverrier, 3248 Cedex 4, France; **nyaitsko@eso.org, phone +49 893200 60; fax +49 89 320 2362, www.eso.org, ESO, Karl-Schwarzschild-Str. 2 D-85748 Garching bei München.